Biomedical Optics EXPRESS

Assessing the imaging performance of light sheet microscopies in highly scattering tissues

A. K. Glaser,[1,*] Y. Wang,[1] and J. T.C. Liu[1]

[1] *Department of Mechanical Engineering, University of Washington, Seattle, WA, USA*
**akglaser@uw.edu*

Abstract: Light sheet microscopy (LSM) has emerged as an optical-imaging method for high spatiotemporal volumetric imaging of relatively transparent samples. While this capability has allowed the technique to be highly impactful in fields such as developmental biology, applications involving highly scattering thick tissues have been largely unexplored. Herein, we employ Monte Carlo simulations to explore the use of LSM for imaging turbid media. In particular, due to its similarity to dual-axis confocal (DAC) microscopy, we compare LSM performance to point-scanned (PS-DAC) and line-scanned (LS-DAC) dual-axis confocal microscopy techniques that have been previously shown to produce high-quality images at round-trip optical lengths of ~9 – 10 and ~3 – 4 respectively. The results of this study indicate that LSM using widefield collection (WF-LSM) provides comparable performance to LS-DAC in thick tissues, due to the fact that they both utilize an illumination beam focused in one dimension (i.e. a line or sheet). On the other hand, LSM using confocal line detection (CL-LSM) is more analogous to PS-DAC microscopy, in which the illumination beam is focused in two dimensions to a point. The imaging depth of LSM is only slightly inferior to DAC (~2 – 3 and ~6 – 7 optical lengths for WF-LSM and CL-LSM respectively) due to the use of a lower numerical aperture (NA) illumination beam for extended imaging along the illumination axis. Therefore, we conclude that the ability to image deeply is dictated most by the confocality of the microscope technique. In addition, we find that imaging resolution is mostly dependent on the collection NA, and is relatively invariant to imaging depth in a homogeneous scattering medium. Our results indicate that superficial imaging of highly scattering tissues using light sheet microscopy is possible.

OCIS codes: (170.1790) Confocal microscopy; (170.2520) Fluorescence microscopy; (170.5810) Scanning microscopy; (110.0113) Imaging through turbid media; (170.3880) Medical and biological imaging.

References and links

1. J. Mertz, "Optical sectioning microscopy with planar or structured illumination," Nat. Methods **8**(10), 811–819 (2011).
2. J. Huisken, J. Swoger, F. Del Bene, J. Wittbrodt, and E. H. K. Stelzer, "Optical sectioning deep inside live embryos by selective plane illumination microscopy," Science **305**(5686), 1007–1009 (2004).
3. C. J. Engelbrecht and E. H. Stelzer, "Resolution enhancement in a light-sheet-based microscope (SPIM)," Opt. Lett. **31**(10), 1477–1479 (2006).
4. H. U. Dodt, U. Leischner, A. Schierloh, N. Jährling, C. P. Mauch, K. Deininger, J. M. Deussing, M. Eder, W. Zieglgänsberger, and K. Becker, "Ultramicroscopy: three-dimensional visualization of neuronal networks in the whole mouse brain," Nat. Methods **4**(4), 331–336 (2007).
5. J. A. Buytaert and J. J. Dirckx, "Design and quantitative resolution measurements of an optical virtual sectioning three-dimensional imaging technique for biomedical specimens, featuring two-micrometer slicing resolution," J. Biomed. Opt. **12**(1), 014039 (2007).
6. P. A. Santi, "Light sheet fluorescence microscopy: a review," J. Histochem. Cytochem. **59**(2), 129–138 (2011).

#254248 Received 20 Nov 2015; revised 8 Jan 2016; accepted 9 Jan 2016; published 14 Jan 2016

7. M. Weber and J. Huisken, "Light sheet microscopy for real-time developmental biology," Curr. Opin. Genet. Dev. **21**(5), 566–572 (2011).
8. E. H. K. Stelzer, S. Lindek, S. Albrecht, R. Pick, G. Ritter, N. J. Salmon, and R. Stricker, "A New Tool for the Observation of Embryos and Other Large Specimens - Confocal Theta-Fluorescence Microscopy," J Microsc-Oxford **179**(1), 1–10 (1995).
9. T. D. Wang, M. J. Mandella, C. H. Contag, and G. S. Kino, "Dual-axis confocal microscope for high-resolution in vivo imaging," Opt. Lett. **28**(6), 414–416 (2003).
10. R. H. Webb and F. Rogomentich, "Confocal microscope with large field and working distance," Appl. Opt. **38**(22), 4870–4875 (1999).
11. J. T. C. Liu, M. J. Mandella, J. M. Crawford, C. H. Contag, T. D. Wang, and G. S. Kino, "Efficient rejection of scattered light enables deep optical sectioning in turbid media with low-numerical-aperture optics in a dual-axis confocal architecture," J. Biomed. Opt. **13**(3), 034020 (2008).
12. J. T. C. Liu, M. J. Mandella, N. O. Loewke, H. Haeberle, H. Ra, W. Piyawattanametha, O. Solgaard, G. S. Kino, and C. H. Contag, "Micromirror-scanned dual-axis confocal microscope utilizing a gradient-index relay lens for image guidance during brain surgery," J. Biomed. Opt. **15**(2), 026029 (2010).
13. J. T. C. Liu, N. O. Loewke, M. J. Mandella, R. M. Levenson, J. M. Crawford, and C. H. Contag, "Point-of-care pathology with miniature microscopes," Anal. Cell Pathol. (Amst.) **34**(3), 81–98 (2011).
14. C. Yin, A. K. Glaser, S. Y. Leigh, L. W. Y. Chen, P. C. S. Pillai, M. C. Rosenberg, S. Abeytunge, G. Peterson, C. Glazowski, N. Sanai, M. J. Mandella, M. Rajadhyaksha, and J. T. C. Liu, "Miniature in vivo MEMS-based line-scanned dual-axis confocal microscope for point-of-care pathology," Biomed. Opt. Express **7**(2), 251–263 (2016).
15. Y. Wu, A. Ghitani, R. Christensen, A. Santella, Z. Du, G. Rondeau, Z. Bao, D. Colón-Ramos, and H. Shroff, "Inverted selective plane illumination microscopy (iSPIM) enables coupled cell identity lineaging and neurodevelopmental imaging in Caenorhabditis elegans," Proc. Natl. Acad. Sci. U.S.A. **108**(43), 17708–17713 (2011).
16. R. McGorty, H. Liu, D. Kamiyama, Z. Dong, S. Guo, and B. Huang, "Open-top selective plane illumination microscope for conventionally mounted specimens," Opt. Express **23**(12), 16142–16153 (2015).
17. P. N. Hedde, M. Stakic, and E. Gratton, "Rapid measurement of molecular transport and interaction inside living cells using single plane illumination," Sci. Rep. **4**, 7048 (2014).
18. E. Baumgart and U. Kubitscheck, "Scanned light sheet microscopy with confocal slit detection," Opt. Express **20**(19), 21805–21814 (2012).
19. P. J. Keller, A. D. Schmidt, J. Wittbrodt, and E. H. Stelzer, "Digital scanned laser light-sheet fluorescence microscopy (DSLM) of zebrafish and Drosophila embryonic development," Cold Spring Harb. Protoc. **2011**(10), 1235–1243 (2011).
20. D. Wang, Y. Chen, Y. Wang, and J. T. C. Liu, "Comparison of line-scanned and point-scanned dual-axis confocal microscope performance," Opt. Lett. **38**(24), 5280–5283 (2013).
21. D. Wang, D. Meza, Y. Wang, L. Gao, and J. T. C. Liu, "Sheet-scanned dual-axis confocal microscopy using Richardson-Lucy deconvolution," Opt. Lett. **39**(18), 5431–5434 (2014).
22. L. Silvestri, A. Bria, L. Sacconi, G. Iannello, and F. S. Pavone, "Confocal light sheet microscopy: micron-scale neuroanatomy of the entire mouse brain," Opt. Express **20**(18), 20582–20598 (2012).
23. Z. Yang, L. Mei, F. Xia, Q. Luo, L. Fu, and H. Gong, "Dual-slit confocal light sheet microscopy for in vivo whole-brain imaging of zebrafish," Biomed. Opt. Express **6**(5), 1797–1811 (2015).
24. S. L. Jacques, "Optical properties of biological tissues: a review," Phys. Med. Biol. **58**(11), R37–R61 (2013).
25. Y. Chen, D. Wang, and J. T. C. Liu, "Assessing the tissue-imaging performance of confocal microscope architectures via Monte Carlo simulations," Opt. Lett. **37**(21), 4495–4497 (2012).
26. Y. Chen and J. T. C. Liu, "Optimizing the performance of dual-axis confocal microscopes via Monte-Carlo scattering simulations and diffraction theory," J. Biomed. Opt. **18**(6), 066006 (2013).
27. D. Wang, Y. Chen, and J. T. C. Liu, "A liquid optical phantom with tissue-like heterogeneities for confocal microscopy," Biomed. Opt. Express **3**(12), 3153–3160 (2012).
28. L. Wang, S. L. Jacques, and L. Zheng, "MCML--Monte Carlo modeling of light transport in multi-layered tissues," Comput. Methods Programs Biomed. **47**(2), 131–146 (1995).
29. Q. Fang and D. A. Boas, "Monte Carlo simulation of photon migration in 3D turbid media accelerated by graphics processing units," Opt. Express **17**(22), 20178–20190 (2009).
30. Q. Fang, "Mesh-based Monte Carlo method using fast ray-tracing in Plücker coordinates," Biomed. Opt. Express **1**(1), 165–175 (2010).
31. A. K. Glaser, S. C. Kanick, R. Zhang, P. Arce, and B. W. Pogue, "A GAMOS plug-in for GEANT4 based Monte Carlo simulation of radiation-induced light transport in biological media," Biomed. Opt. Express **4**(5), 741–759 (2013).
32. P. Arce, J. I. Lagares, L. Harkness, D. Perez-Astudillo, M. Canadas, P. Rato, M. de Prado, Y. Abreu, G. de Lorenzo, M. Kolstein, and A. Diaz, "GAMOS: A framework to do GEANT4 simulations in different physics fields with an user-friendly interface," Nucl Instrum Meth A **735**, 304–313 (2014).
33. P. K. Milsom, "A ray-optic, Monte Carlo, description of a Gaussian beam waist - applied to reverse saturable absorption," Appl. Phys. B **70**(4), 593–599 (2000).

#254248 Received 20 Nov 2015; revised 8 Jan 2016; accepted 9 Jan 2016; published 14 Jan 2016

34. B. H. Hokr, J. N. Bixler, G. Elpers, B. Zollars, R. J. Thomas, V. V. Yakovlev, and M. O. Scully, "Modeling focusing Gaussian beams in a turbid medium with Monte Carlo simulations," Opt. Express **23**(7), 8699–8705 (2015).
35. R. J. Crilly, W. F. Cheong, B. Wilson, and J. R. Spears, "Forward-adjoint fluorescence model: Monte Carlo integration and experimental validation," Appl. Opt. **36**(25), 6513–6519 (1997).
36. J. Chen and X. Intes, "Comparison of Monte Carlo methods for fluorescence molecular tomography-computational efficiency," Med. Phys. **38**(10), 5788–5798 (2011).
37. A. R. Gardner, C. K. Hayakawa, and V. Venugopalan, "Coupled forward-adjoint Monte Carlo simulation of spatial-angular light fields to determine optical sensitivity in turbid media," J. Biomed. Opt. **19**(6), 065003 (2014).
38. P. J. Keller, A. D. Schmidt, A. Santella, K. Khairy, Z. Bao, J. Wittbrodt, and E. H. K. Stelzer, "Fast, high-contrast imaging of animal development with scanned light sheet-based structured-illumination microscopy," Nat. Methods **7**(8), 637–642 (2010).
39. Z. Lavagnino, F. C. Zanacchi, E. Ronzitti, and A. Diaspro, "Two-photon excitation selective plane illumination microscopy (2PE-SPIM) of highly scattering samples: characterization and application," Opt. Express **21**(5), 5998–6008 (2013).
40. F. Cella Zanacchi, Z. Lavagnino, M. Faretta, L. Furia, and A. Diaspro, "Light-sheet confined super-resolution using two-photon photoactivation," PLoS One **8**(7), e67667 (2013).
41. L. Gao, L. Zhu, C. Li, and L. V. Wang, "Nonlinear light-sheet fluorescence microscopy by photobleaching imprinting," J. R. Soc. Interface **11**(93), 20130851 (2014).
42. M. Abdellah, A. Bilgili, S. Eilemann, H. Markram, and F. Schürmann, "Physically-based in silico light sheet microscopy for visualizing fluorescent brain models," BMC Bioinformatics **16**(Suppl 11), S8 (2015).
43. E. Mei, P. A. Fomitchov, R. Graves, and M. Campion, "A line scanning confocal fluorescent microscope using a CMOS rolling shutter as an adjustable aperture," J. Microsc. **247**(3), 269–276 (2012).
44. A. Rohrbach, "Artifacts resulting from imaging in scattering media: a theoretical prediction," Opt. Lett. **34**(19), 3041–3043 (2009).
45. Y. Chen and J. T. C. Liu, "Characterizing the beam steering and distortion of Gaussian and Bessel beams focused in tissues with microscopic heterogeneities," Biomed. Opt. Express **6**(4), 1318–1330 (2015).
46. I. R. Capoğlu, A. Taflove, and V. Backman, "Computation of tightly-focused laser beams in the FDTD method," Opt. Express **21**(1), 87–101 (2013).
47. A. Elmaklizi, J. Schäfer, and A. Kienle, "Simulating the scanning of a focused beam through scattering media using a numerical solution of Maxwell's equations," J. Biomed. Opt. **19**(7), 071404 (2014).
48. A. Elmaklizi, D. Reitzle, A. Brandes, and A. Kienle, "Penetration depth of focused beams in highly scattering media investigated with a numerical solution of Maxwell's equations in two dimensions," J. Biomed. Opt. **20**(6), 065007 (2015).
49. T. A. Planchon, L. Gao, D. E. Milkie, M. W. Davidson, J. A. Galbraith, C. G. Galbraith, and E. Betzig, "Rapid three-dimensional isotropic imaging of living cells using Bessel beam plane illumination," Nat. Methods **8**(5), 417–423 (2011).
50. F. O. Fahrbach and A. Rohrbach, "Propagation stability of self-reconstructing Bessel beams enables contrast-enhanced imaging in thick media," Nat. Commun. **3**, 632 (2012).
51. F. O. Fahrbach, V. Gurchenkov, K. Alessandri, P. Nassoy, and A. Rohrbach, "Light-sheet microscopy in thick media using scanned Bessel beams and two-photon fluorescence excitation," Opt. Express **21**(11), 13824–13839 (2013).
52. T. Vettenburg, H. I. Dalgarno, J. Nylk, C. Coll-Lladó, D. E. Ferrier, T. Čižmár, F. J. Gunn-Moore, and K. Dholakia, "Light-sheet microscopy using an Airy beam," Nat. Methods **11**(5), 541–544 (2014).

1. Introduction

Light sheet fluorescence microscopy (LSM) has emerged as an important optical-imaging technique that provides some degree of optical sectioning and rejection of out-of-focus light for relatively transparent specimens, but with the added benefit of improved imaging speeds, reduced photobleaching, and larger fields of view as compared to alternatives such as confocal laser scanning microscopy (CLSM) and two-photon microscopy [1]. To date, LSM has had the most impact in fields such as developmental biology, where studies have focused primarily on the imaging of transparent or optically cleared specimens due to geometric constraints (i.e. only small samples may be mounted in a gel and imaged at the intersection of orthogonally arranged illumination and collection beams), and degradation of image quality due to beam-steering and light scattering [2–7]. Due to these limitations, there has been little investigation into the feasibility of using LSM to image samples that are highly scattering, such as most human tissues. However, the LSM imaging geometry is similar to dual-axis confocal (DAC) microscopy methods (both may be viewed as natural developments of the confocal theta microscope proposed by Stelzer et. al. [8]), which have successfully been

#254248 Received 20 Nov 2015; revised 8 Jan 2016; accepted 9 Jan 2016; published 14 Jan 2016

utilized for reflectance and fluorescence imaging of thick, highly scattering tissues in a number of *ex-vivo* and *in-vivo* studies [9–14]. Furthermore, recent reports have demonstrated LSM in novel "open-top" or "inverted" imaging geometries that are more compatible for the imaging of conventionally mounted specimens of arbitrary size [15–17], as well as the use of confocal line detection for improved contrast in scattering samples [18]. Given these recent developments in LSM, the similarity of LSM to DAC microscopy, and the ability of DAC microscopy to provide high-quality fluorescence images of highly scattering tissues, here we assess the performance of LSM for imaging large and highly scattering *in-vivo* and *ex-vivo* tissues using Monte Carlo simulations.

2. DAC and LSM imaging geometries

To highlight the similarity between the DAC and LSM techniques, we present representative illustrations of a point-scanned dual-axis confocal microscope (PS-DAC), line-scanned dual-axis confocal microscope (LS-DAC), wide-field detection light-sheet microscope (WF-LSM), and confocal line detection light-sheet microscope (CL-LSM) in Fig. 1.

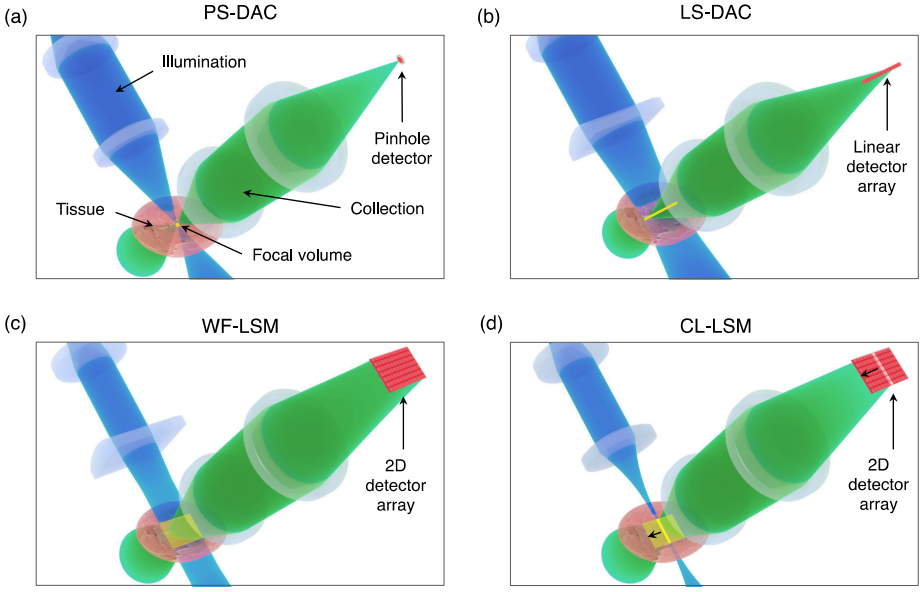

Fig. 1. The illumination, collection, focal volume, and detector configurations for the PS-DAC, LS-DAC, WF-LSM, and CL-LSM microscope geometries. In (a), the PS-DAC geometry uses a moderate numerical aperture to illuminate a single point within the tissue, and a similar collection NA to image that point to a pinhole detector. In (b), the LS-DAC geometry uses a moderate illumination NA focused to a line, rather than a point within the tissue volume. This focal line is then imaged onto a linear detector array. In (c), the WF-LSM geometry uses a low illumination NA to provide a sheet of illumination (a low-NA line focus) within the tissue volume, which is imaged with a higher NA onto a two-dimensional (2D) image sensor. In (d), the CL-LSM geometry is shown, in which an illumination sheet identical to that in (c) is created over time by scanning a low-NA point-focused illumination beam, which is synchronized with the rolling shutter (line-by-line acquisition) of a 2D image sensor.

In Fig. 1(a), the geometry for a PS-DAC system is shown. A moderate illumination and collection numerical aperture (NA) ~0.15 – 0.25 are used to illuminate and collect signal from a point within the tissue, and to image that focal point onto a pinhole detector, respectively. This configuration is fully confocal in all three dimensions, but images only a point and requires scanning in two dimensions to build a two-dimensional (2D) image. The LS-DAC

#254248 Received 20 Nov 2015; revised 8 Jan 2016; accepted 9 Jan 2016; published 14 Jan 2016

geometry is shown in Fig. 1(b). Again a moderate illumination NA ~0.15 – 0.25 (is utilized. However, in this case, a line focus is illuminated within the tissue volume (by using cylindrical focusing optics), which is imaged onto a linear detector array. In this case, the focal line only needs to be scanned in one dimension to build a 2D image, allowing for increased imaging speeds at the cost of a loss in confocality along one dimension. In Figs. 1(c) and 1(d), the WF-LSM and CL-LSM configurations are shown. For both, a low illumination NA < 0.10 is used to provide a sheet of illumination with a long depth of focus within the tissue while a moderate or high NA (greater than the illumination NA) is used for collection. For WF-LSM, the illumination sheet is created directly with cylindrical optics or indirectly by scanning a spherically focused beam [19], and a 2D image is captured of the entire light sheet. The CL-LSM configuration is analogous to WF-LSM using a scanned beam, except in this case the scan is synchronized with the rolling shutter (line-by-line acquisition) of a 2D detector array to indirectly image a sheet within the tissue, where the successive lines of active pixels during the camera readout serve as linear-array detectors. The benefit of this latter configuration, in comparison to WF-LSM, is that confocal detection is achieved along two dimensions (all except the illumination axis) [18].

3. Methods

3.1 A generalized imaging geometry for Monte Carlo simulations

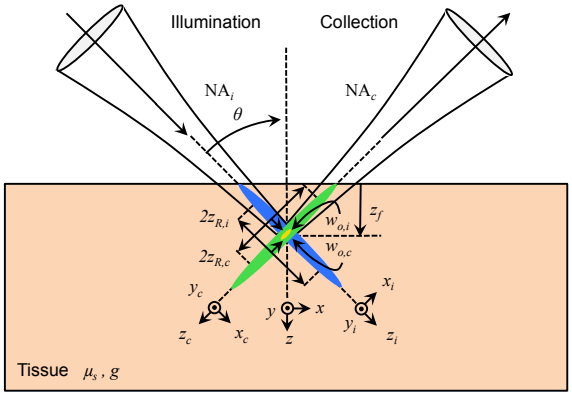

Fig. 2. The general microscope geometry for the DAC and LSM methods is shown. The illumination beam (blue) enters the tissue from the left, at an angle θ from the normal, along the illumination coordinate axes denoted by x_i, y_i, and z_i. Similarly, light is collected (green) to the right at an angle θ from the normal, along the collection coordinate axes x_c, y_c, and z_c. The effective focal volume is shown for illustrative purposes (yellow). The numerical aperture of each optical path is given by NA$_i$ and NA$_c$ respectively, which dictates the corresponding beam waists, $w_{o,i}$ and $w_{o,c}$ and Rayleigh ranges $z_{R,i}$ and $z_{R,c}$. Both beams are focused at a depth, z_f, into tissue with scattering coefficient μ_s, and scattering anisotropy, g. The coordinate axes of the tissue are given by x, y, and z.

Given the similarities of the DAC and LSM configurations, the generalized imaging geometry shown in Fig. 2 can be used to describe all four techniques for simulation purposes. An illumination beam enters the tissue from the left, exciting fluorescence, which is collected to the right by a collection lens. The NA of the illumination and collection paths are given by NA$_i$ and NA$_c$ respectively, and the half-crossing angle of both beams relative to the normal of the tissue, θ, is 45 degrees, i.e. the illumination and collection are perpendicular to one another, a fundamental property of LSM. This differs slightly from the previously reported DAC methods, in which θ = 30 degrees, but for the purposes of comparison using the generalized imaging geometry, in this study θ = 45 degrees was used for all DAC and LSM simulations [9–14, 20, 21]. Therefore, the only fundamental differences between the four

#254248 Received 20 Nov 2015; revised 8 Jan 2016; accepted 9 Jan 2016; published 14 Jan 2016

imaging methods lies in the shape of the illumination beam (point focusing for PS-DAC and CL-LSM vs. line focusing for LS-DAC and WF-LSM), the detection scheme (see Fig. 1), and the illumination numerical aperture, NA_i (although NA_c may also vary slightly). For a Gaussian beam, the NA dictates the radius of the beam waist, $w_o = \lambda/\pi NA$, and the Rayleigh range, $z_R = w_o^2\pi/\lambda$, which provides a measure of the depth of focus (given by $2z_R$) along the illumination axis, z_i. As is well-known for Gaussian beams, there exists a fundamental trade-off between the thickness and depth of focus of the beam, which is plotted in Fig. 3. Note that while there is a dependence of both parameters on the wavelength (λ), a single wavelength of 500 nm was used as a representative wavelength for all cases in this study.

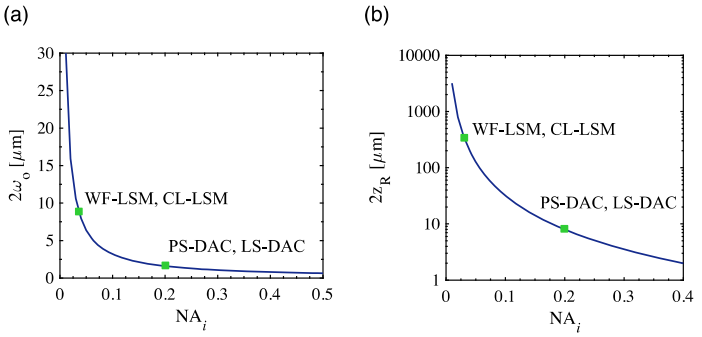

Fig. 3. In (a) and (b), the illumination beam thickness, $2w_o$ and depth of focus, $2z_R$ are plotted for the PS-DAC, LS-DAC, WF-LSM, and CL-LSM microscope geometries, respectively.

The NAs used for the simulations of each microscope geometry, and the corresponding beam waists and Rayleigh ranges are denoted in Fig. 3 and summarized in Table 1. For the PS-DAC geometry, NA_i and NA_c of 0.20 were used, similar to previous reports [9–13]. The LS-DAC geometry was identical to the PS-DAC geometry, except that in this case (as described previously) a line of illumination was used, i.e. focusing was performed in the x_i dimension only, which allows for direct imaging along the y_i dimension [14, 20, 21]. Similarly, for WF-LSM, a low NA_i of 0.03 (focused only in the x_i dimension), coupled to a higher collection NA_c of 0.30 was used, similar to what has been used previously by other groups [2–4, 16]. This reduction in NA_i results in an extended Rayleigh range ($z_{R,i}$) along the z_i axis which allows for the direct imaging of a 2D sheet oriented in the y_i-z_i plane, with a correspondingly larger beam waist ($w_{o,i}$). Finally, the CL-LSM geometry is similar to the WF-LSM geometry, except that the illumination beam is now focused along both the x_i and y_i dimensions, and is scanned along the y_i direction in order to create an indirect light sheet over time. For CL-LSM, it is assumed that a rolling shutter is used for line-by-line confocal imaging of a light sheet [18, 22, 23]. Irrespective of the NAs, the geometric focus of the illumination and collection beams are centered at a focal depth, z_f, inside a thick tissue with a scattering coefficient, μ_s, and scattering anisotropy, g. For this study, a range of focal depths were studied to assess imaging performance as a function of depth in tissue (50 – 450 μm in 50 μm increments), the scattering coefficient was assumed to be 10 mm^{-1}, and the scattering anisotropy 0.9, which are representative of a generic human tissue [24]. For generalization to other scattering properties and imaging depths, the focal depth and scattering coefficient can also be incorporated into a dimensionless optical length, defined as $L = 2\mu_s z_f$, which is equal to the total number of mean free paths traversed by ballistic photons on a perpendicular round-trip path from the tissue surface to the focus. The values of z_f and μ_s used in this study correspond to optical lengths of L = 1, 3, 5, 7, and 9. Finally, simulations were also performed in the absence of a tissue sample (no scattering) to assess the ideal performance of each microscope geometry, i.e. L = 0. Note that for simplicity, the refractive index mismatch

#254248 Received 20 Nov 2015; revised 8 Jan 2016; accepted 9 Jan 2016; published 14 Jan 2016

between the tissue and the surrounding air was not modeled, i.e. only the effects of tissue scattering on ideally focused beams were investigated and aberrations were not considered.

Table 1. Summary of simulation parameters used for each microscope geometry at λ = 500 nm

Microscope geometry	Refs.	Focusing direction(s)	NA_i	$2w_{o,i}$ [μm]	$2z_{R,i}$ [μm]	NA_c	$2w_{o,c}$ [μm]	$2z_{R,c}$ [μm]
PS-DAC	[9–13]	x_i and y_i	0.20	1.60	7.96	0.20	1.60	7.96
LS-DAC	[14, 20, 21]	x_i only	0.20	1.60	7.96	0.20	1.60	7.96
WF-LSM	[2–4, 16]	x_i only	0.03	10.62	353.68	0.30	1.06	3.54
CL-LSM	[18, 22, 23]	x_i and y_i	0.03	10.62	353.68	0.30	1.06	3.54

3.2 Simulation architecture

Previous Monte Carlo characterizations of DAC performance in scattering media have utilized a commercially available optical simulation software (FRED, Photon Engineering, Tucson, AZ) [11, 25, 26]. This approach has the advantage that accurate ray tracing can be performed along an entire optical circuit (from source to detector), modeling aberrations intrinsic to a specific optical system. However, the software cannot model the diffraction effects of a focused Gaussian beam while running in a Monte-Carlo simulation mode (i.e., the rays in a transparent medium will not be distributed within a finite beam waist, but will instead converge to an exact focus, which is not realistic). While the effects of a diffraction-limited spot size in a scattering medium may be negligible in the fully diffuse regime ($L >> 10$), for the optical lengths investigated in this study ($L \leq 9$) the light transport contains a mixture of ballistic and diffuse light, and accurate modeling of the finite Gaussian spot size provides more accurate results. Furthermore, since FRED is not well equipped to model fluorescence in an efficient manner, only reflectance-based imaging was modeled in previous studies. While this previous method was amenable to experimental validation (e.g. with Intralipid and bead phantoms) [27], our current study utilizes an alternative approach to model the performance of a fluorescence-based system.

A number of Monte Carlo codes have been developed for the simulation of light transport in scattering media, (e.g., MCML, MCX, MMC) [28–30]. However, here we employ the GEANT4 architecture for medically oriented simulations (GAMOS) due to its flexibility, ease of use, and recent extension to tissue optics [31, 32]. In particular, we have further extended its functionality to microscopy applications by incorporating a ray-optic model that accurately simulates the propagation of a focused Gaussian beam. The details of the method for modeling a focused beam are provided elsewhere, but in short, an accurate focused Gaussian spot is generated by modeling the positional and directional distribution of the rays at the pupil plane and beam focus [33, 34]. To validate this Gaussian-modeling method, we simulated the 2D irradiance distribution for a focused Gaussian beam in air with $NA_x = NA_y = 0.10$ at $\lambda = 500$ nm, and compared it to the analytical form of the beam intensity predicted by Gaussian beam optics. The results are shown in 4(a). The expected beam waist, $w_o = 1.59$ μm is in close agreement with the simulated beam waists in the x and y directions, $w_{o,x} = w_{o,y} = 1.60$ μm.

To accurately and efficiently model fluorescence detection, we employed the widely used adjoint method [35–37], in which the illumination and collection beams are both treated as illumination beams, and the product of the simulated illumination beam irradiance profile, S_i, and collection beam profile, S_c, at every image voxel yields the point spread function, $S_{i,c}$ (PSF) of the microscope in the presence of scattering. For each simulation, we recorded the response functions in a $100 \times 100 \times 100$ μm^3 scoring volume, with a voxel size of 0.25×0.25

#254248 Received 20 Nov 2015; revised 8 Jan 2016; accepted 9 Jan 2016; published 14 Jan 2016

× 0.25 μm^3 and 10^6 total rays. Each S_i or S_c simulation was run on a computer running Linux (single processor - AMD Opteron 4386, 3.1GHz), with a simulation time ranging from 3 – 24 minutes depending on the given focal depth and NA. Finally, we calculated 3D PSFs for each imaging method as a function of the various optical lengths, $S_{i,c}(x,y,z,L)$. A representative schematic of the adjoint method is shown in Fig. 4(b).

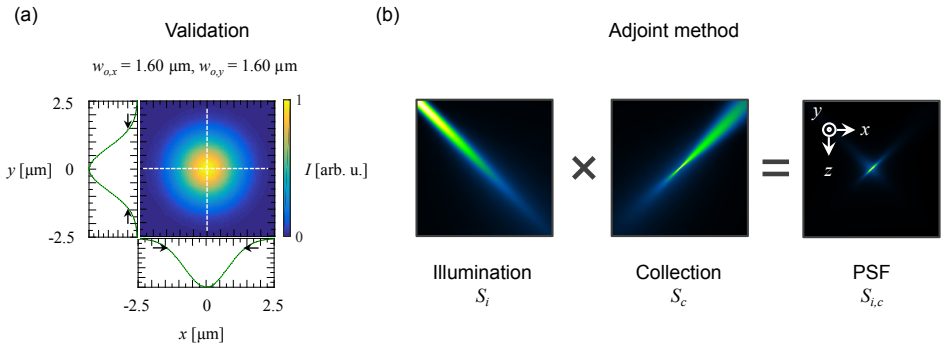

Fig. 4. In (a), using a ray-optics model that accurately simulates Gaussian beam profiles, the irradiance profile is simulated at the focal plane of a beam with $NA_x = NA_y = 0.10$ at $\lambda = 500$ nm, along with plots of the x and y line profiles through the focus. The measured beam waists, $w_{o,x} = w_{o,y} = 1.60$ μm, are in close agreement to the expected beam waist of 1.59 μm. In (b), the principle of the adjoint method is shown, where the PSF, $S_{i,c}$ is calculated by multiplying the illumination fluence, S_i, by the reversed collection fluence, S_c.

3.3 PSF analysis

To evaluate the effect of scattering on resolution, line profiles along the x, y, and z axis through the center of various simulated PSFs were plotted. The full-width at half-max (FWHM) width of the PSFs were quantified as a function of optical scattering. It is important to note that while in traditional LSM studies, the response is often analyzed along the $x_{i,c}$, $y_{i,c}$ and $z_{i,c}$ directions, when imaging in a thick tissue using an "open-top" or "inverted" configuration, the response in the tissue's x, y, and z coordinates is more appropriate to evaluate. In addition, to evaluate the optical-sectioning performance of each microscopy geometry, the axial response of the system to a planar object was calculated by summing the PSF in the x-y plane, and plotting this sum as a function of axial distance, z, from the focal plane for each optical length, thus yielding $S_{i,c}(z,L)$ for each microscope geometry. This is analogous to the axial response (reflectance) to a plane mirror, except in this case the axial response to a thin fluorescence sheet is simulated. Finally, the signal-to-background ratio (SBR) was evaluated by taking the ratio of $S_{i,c}$ at the focus, and at the end of the axial scan where the planar sheet is translated far from the focus (i.e. the 'signal' is considered the peak value of the PSF, and the 'background' is taken as the value of the PSF at the edge of the axial scan).

3.4 Fluorescent bead phantom

Since the adjoint-method Monte Carlo simulations yield a full 3D PSF, it is possible to calculate the response of the modeled systems to any arbitrary fluorescence source distribution. In particular, it is straightforward to simulate the imaging response to a fluorescent bead phantom, a technique that has been commonly used experimentally in LSM and other methods to evaluate the effects of scattering and other parameters on microscope performance [38–41]. To realize this, we initialized a digital phantom, $P(x,y,z)$, with a scattering coefficient and anisotropy analogous to that of the tissue phantom used to generate the PSFs (μ_s = 10 mm^{-1}, g = 0.9), which is 200 × 200 × 450 μm^3 in size, with a voxel size of 0.25 × 0.25 × 0.25 μm^3. The values at all voxels were first set to 0 (i.e. no fluorescence), and

#254248 Received 20 Nov 2015; revised 8 Jan 2016; accepted 9 Jan 2016; published 14 Jan 2016

sub-resolution fluorescent beads were then randomly distributed inside the phantom by setting groups of voxels to 1 at a "concentration" of 1% v/v. With the voxel size in all simulations set to 0.25 μm, this is equivalent to using 250 nm diameter beads, which is below the diffraction limit at the NA_c values used in this study. The simulated imaging performance for each microscopy geometry can then be approximated by convolving the PSF at a given optical length, L_p (or depth, z_p) with the phantom: $I(x,y,z) = P(x,y,z_p) \cdot S_{i,c}(x,y,z,L_p)$. The contrast as a function of z_p was then evaluated over the entire xy plane as $C = (I_{max} - I_{min})/(I_{max} + I_{min})$ for each microscope geometry.

3.5 Varying illumination and collection numerical aperture

In order to fully explore the parameter space of the generalized imaging geometry, simulations were also executed to calculate the PSF as a function of optical length for a wider array of illumination and collection numerical aperture combinations (NA_i = 0.01, 0.03, 0.05, 0.07, and 0.09 and NA_c = 0.10, 0.20, 0.30, 0.40, and 0.50). The FWHM of the resulting PSFs were calculated to assess the effect of NA_i or NA_c on resolution, and the fluorescent bead phantom procedure described in Sec. 3.4 was used to assess the effect of NA_i or NA_c on the imaging contrast.

4. Results

4.1 Effect of scattering on PSF

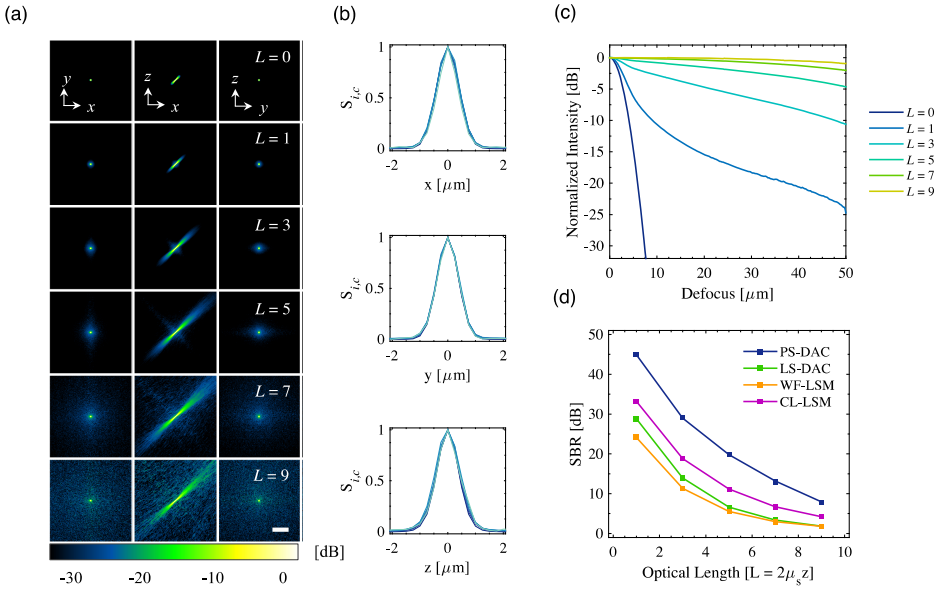

Fig. 5. In (a), the PSFs, $S_{i,c}(x,y,z,L)$, are shown for the WF-LSM geometry. Each is self-normalized and displayed on a dB scale ($10\log_{10}$) down to −30 dB (10^{-3}). In (b), the corresponding x, y, and z line profiles through the focus are plotted for each optical length, L. The corresponding axial scans $S_{i,c}(z,L)$ are shown in (c). In (d), the contrast (SBR) of the PS-DAC, LS-DAC, WF-LSM, and CL-LSM are plotted as a function of optical length. The scale bar in (a) represents 20 μm.

The PSF results for the WF-LSM microscope geometry are shown in Fig. 5. The self-normalized x-y, x-z, and y-z cross-sections of the PSF for all optical lengths are shown in Fig. 5(a) from −30 to 0 dB ($10\log_{10}$) scale). In the x-z plane, the asymmetric PSF is due to the large difference in NA_i and NA_c and corresponding $2w_{o,i}$ and $2w_{o,c}$ (10.62 and 1.06 μm respectively). As expected, as the optical length is increased, the corresponding background signal around the original PSF grows both in magnitude and extent due to increased optical

#254248 Received 20 Nov 2015; revised 8 Jan 2016; accepted 9 Jan 2016; published 14 Jan 2016

scattering. However, as has been shown previously using Monte Carlo simulations of DAC microscope geometries, analysis of the PSF along the x, y, and z axes reveals that the full-width at half-maximum (FWHM) in all three directions does not degrade with increasing optical length, $FWHM_x = 0.98 \pm 0.04$ μm, $FWHM_y = 0.97 \pm 0.07$ μm, $FWHM_z = 0.98 \pm 0.04$ μm [25, 26]. The corresponding fluorescence axial scan, $S_{i,c}(z,L)$, for the WF-LSM geometry is plotted in Fig. 5(c). As can be seen on the dB scale, the background signal outside of the central lobe of the PSF increases as a function of optical length. A corresponding decrease in the SBR is apparent as the optical length is increased. Similar results as those shown in Figs. 5(a)-5(c) were obtained for the other three imaging geometries. This information, for all four microscope geometries, can be summarized by plotting the SBR as a function of optical length, as shown in Fig. 5(d). The highest SBR is achieved by the PS-DAC geometry, followed by the CL-LSM, LS-DAC, and WF-LSM geometries.

3.2 Effect of scattering on imaging contrast

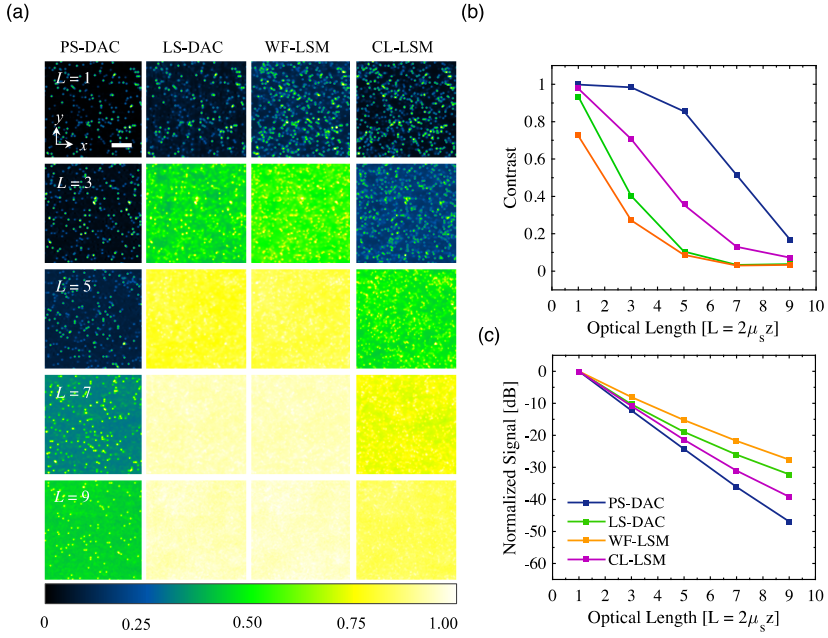

Fig. 6. For each microscopy method, x-y sections of a fluorescent bead phantom, convolved with the appropriate PSF, are shown in (a), self normalized to a maximum value of 1.0. In (b) and (c), the calculated contrast of the images is plotted, as well as the decay in the peak signal of the PSFs as a function of optical length. The scale bar in (a) represents 20 μm.

The results of the simulated fluorescent bead phantom images are shown in Fig. 6(a) for the PS-DAC, LS-DAC, WF-LSM, and CL-LSM microscope geometries at optical lengths of L = 1, 3, 5, 7, and 9. Each image is self-normalized such that the maximum pixel value is equal to 1. The images reveal a number of interesting features. As expected from the SBR plot, the PS-DAC geometry is able to maintain the highest contrast even at an optical length of 9. Although the contrast is reduced due to the increasing background, the beads are still visible. This is in comparison to the LS-DAC and WF-LSM geometries, where an image of equivalent contrast is reached at an optical length of just 3. By re-establishing confocality in the y dimension, the CL-LSM microscope geometry is able to obtain better contrast relative to the WF-LSM microscope geometry. An image of comparable contrast to the WF-LSM at an optical length of 3 is obtained by the CL-LSM at an optical length of 5. However, with the exception of the PS-DAC geometry, all other geometries are unable to form a usable image past an optical length of 5. The resulting plot of contrast as a function of optical length,

#254248 Received 20 Nov 2015; revised 8 Jan 2016; accepted 9 Jan 2016; published 14 Jan 2016

calculated from the planar fluorescent bead images, is shown in Fig. 6(b). Finally, in Fig. 6(c) the un-normalized peak signal of the PSFs of each microscopy geometry is plotted as a function of optical length. For the PS-DAC configuration, the peak signal decays exponentially at a rate of $1/(L\cos\theta)$ corresponding to exponential attenuation (Beer-Lambert law) due to scattering of the ballistic photons. On the other hand, the rate of peak-signal decay is decreased for the CL-LSM, LS-DAC, and WF-LSM systems (deviation from Beer-Lambert law decay) due to increased collection of background photons as the optical length is increased.

4.3 Effect of illumination and collection numerical aperture

The FWHM of the PSFs as a function of the array of NA_i and NA_c combinations are shown in Table 2 for the *x*, *y*, and *z* directions respectively. As in the representative case shown in Fig. 5, the FWHM is largely independent of scattering and optical length. The standard deviation in FWHM across all optical lengths for each configuration is denoted in the table. While the results for the resolution as a function of the NAs in Table 2 is for WF-LSM specifically, the results for the CL-LSM configuration are equivalent (except for a slight change in FWHM along the *y* axis due to the difference between a cylindrically or spherically focused illumination beam). This slight difference has been discussed previously for PS-DAC and LS-DAC microscopes [20]. Table 2 also highlights that for the LSM regime (i.e., $NA_i < NA_c$) the FWHM is dictated mostly by the higher NA_c.

Table 2. Summary of the FWHM values as a function of NA_i and NA_c for WF-LSM for the *x* (top), *y* (middle), and *z* (bottom) directions

FWHM [μm]		NA_c				
		0.10	0.20	0.30	0.40	0.50
NA_i	0.01	*x*: 2.81 ± 0.07	1.43 ± 0.04	0.96 ± 0.03	0.77 ± 0.01	0.66 ± 0.01
		y: 2.82 ± 0.17	1.36 ± 0.03	0.97 ± 0.07	0.75 ± 0.01	0.65 ± 0.01
		z: 2.78 ± 0.07	1.43 ± 0.06	1.00 ± 0.05	0.77 ± 0.06	0.64 ± 0.06
	0.03	2.74 ± 0.14	1.37 ± 0.05	0.98 ± 0.04	0.76 ± 0.03	0.65 ± 0.03
		2.82 ± 0.17	1.36 ± 0.03	0.97 ± 0.07	0.75 ± 0.01	0.65 ± 0.01
		2.69 ± 0.12	1.38 ± 0.07	0.98 ± 0.04	0.76 ± 0.05	0.65 ± 0.05
	0.05	2.64 ± 0.19	1.36 ± 0.04	0.94 ± 0.04	0.77 ± 0.02	0.66 ± 0.02
		2.82 ± 0.17	1.36 ± 0.03	0.97 ± 0.07	0.75 ± 0.01	0.65 ± 0.01
		2.59 ± 0.16	1.36 ± 0.07	0.97 ± 0.04	0.81 ± 0.05	0.72 ± 0.04
	0.07	2.50 ± 0.23	1.34 ± 0.03	0.93 ± 0.03	0.76 ± 0.02	0.65 ± 0.02
		2.82 ± 0.17	1.36 ± 0.03	0.97 ± 0.07	0.75 ± 0.01	0.65 ± 0.01
		2.48 ± 0.21	1.34 ± 0.05	0.96 ± 0.03	0.77 ± 0.05	0.66 ± 0.04
	0.09	2.32 ± 0.24	1.32 ± 0.02	0.93 ± 0.02	0.76 ± 0.01	0.65 ± 0.01
		2.82 ± 0.17	1.36 ± 0.03	0.97 ± 0.07	0.75 ± 0.01	0.65 ± 0.01
		2.34 ± 0.29	1.34 ± 0.05	0.97 ± 0.05	0.76 ± 0.07	0.66 ± 0.06

The contrast values as a function of optical length in the fluorescent bead phantom for WF-LSM and CL-LSM are shown in Fig. 7, for various combinations of NAi and NAc. For WF-LSM, using a fixed NAc = 0.30 with an increasing NAi from 0.01 to 0.09 provides performance that approaches that of the LS-DAC case, in which NAi = NAc = 0.20. The corresponding results for a fixed NAi = 0.03, while varying NAc from 0.10 to 0.50, are shown in Fig. 7(b). While the performance is increased as a function of increasing NAc, the improvement is less dramatic than the improvement due to an increase in NAi.

Similar results for CL-LSM are shown in Figs. 7(c) and 7(d). For a fixed $NA_c = 0.30$, increasing NA_i from 0.01 to 0.09 shows performance which approaches that of the PS-DAC case where $NA_i = NA_c = 0.20$. Again, although the imaging performance is improved by

#254248 Received 20 Nov 2015; revised 8 Jan 2016; accepted 9 Jan 2016; published 14 Jan 2016

increasing NA_c at a fixed $NA_i = 0.03$, the improvement is not as significant as increasing NA_i. Therefore, for LSM, contrast is dictated mostly by NA_i, which is typically much lower than NA_c.

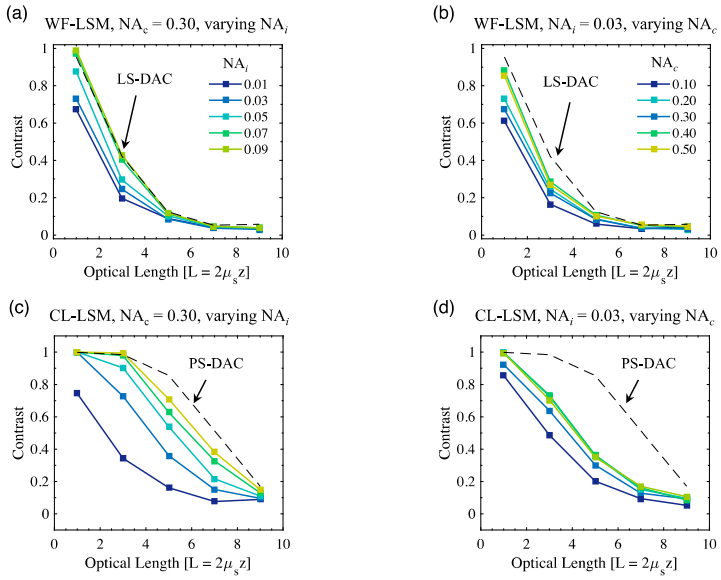

Fig. 7. Image contrast values as a function of optical length in the fluorescent bead phantom are plotted for: (a) WF-LSM as a function of NA_i for a fixed $NA_c = 0.30$, (b) WF-LSM as a function of NA_c for a fixed $NA_i = 0.03$, (c) CL-LSM as a function of NA_i for a fixed $NA_c = 0.30$, (b) CL-LSM as a function of NA_c for a fixed $NA_i = 0.03$. For (a-b), the dashed line represents the performance of LS-DAC where $NA_i = NA_c = 0.20$, and in (c-d) the dashed line represents the performance of PS-DAC where $NA_i = NA_c = 0.20$.

4. Discussion and conclusions

We have utilized Monte Carlo simulations to quantitatively assess the performance of LSM in comparison to previous DAC methods for the imaging of highly scattering tissues. By using a customized version of the GAMOS tissue-optics plug-in to GEANT4, the responses of LSM and DAC microscope geometries have been modeled with the ability to account for the finite spot size of a focused Gaussian beam, as well as fluorescence detection (using the adjoint method). In agreement with previous studies, the results of this study show minimal change in the FWHM of the PSFs in the *x*, *y*, and *z* directions as a function of increasing optical length. For a LSM system, the FWHM is instead dictated primarily by NA_c, as is highlighted by the results presented in Table 2. Finally, for all imaging geometries, as would be expected, the contrast (SBR) was found to decrease significantly with increasing optical length, as is shown in Fig. 5(d).

It is often difficult to visualize how optical simulations translate to actual imaging performance. Therefore, due to the fact that the adjoint method used in this study results in a full 3D PSF, the PSFs for each imaging method were convolved with a digital phantom containing sub-resolution fluorescent beads to produce *in-silico* imaging results. This is similar to the methodology of a recent study by Abdellah et. al. on the development of a computational workflow for *in-silico* analysis of LSM for brain models [42]. The simulated images of this study were used to generate plots of image contrast (SBR) as a function of optical length, which highlights the achievable imaging depth in tissue for each microscope geometry. For PS-DAC microscopy, the maximum imaging depth was found to be approximately ~9 – 10 round-trip optical lengths, in agreement with previous experimental

#254248 Received 20 Nov 2015; revised 8 Jan 2016; accepted 9 Jan 2016; published 14 Jan 2016

reports where images were obtained to a depth of ~450 – 500 μm in esophageal tissue (assuming a scattering coefficient of ~10 mm^{-1}) [11]. For LS-DAC microscopy, the ultimate imaging depth was found to be ~3 – 4 optical lengths, also in agreement with a recent experimental study where a LS-DAC system was able to image down to an optical length of ~4 in *ex-vivo* mouse tissue [20]. While there exists no thorough experimental studies in highly scattering tissues for which the WF-LSM simulations can be compared, the results suggest that imaging performance would be comparable to LS-DAC (in that an ultimate imaging depth of ~2 – 3 optical lengths may be achieved). However, the resolution of a WF-LSM microscope in the *z* direction would be degraded slightly due to the asymmetric, elongated PSF shown in Fig. 5(a). This is somewhat visible in Fig. 6(a), where the optical sectioning of the WF-LSM system at an optical length of 1 is worse than that of the LS-DAC system (i.e., more out-of-plane beads are visible).

The CL-LSM method exhibits significantly improved imaging performance and rejection of background signal, compared with the LS-DAC and WF-LSM methods, due to additional confocality in the *y* dimension. This allows for deeper imaging down to optical lengths of ~6 – 7, or an approximate doubling in contrast at any given optical length over WF-LSM. This is in agreement with initial reports comparing CL-LSM to WF-LSM [43]. Therefore, while NA_i has an impact on the image contrast, and NA_c primarily dictates the resolving power of the various microscope geometries, the limiting factor when imaging in thick tissues is the suppression of background signal that can be achieved by introducing confocality along various dimensions. Interestingly, in this study this takes the form of a first tier of imaging performance for PS-DAC and CL-LSM, where there is confocality in the *x*, *y*, and *z* dimensions, and a second tier for LS-DAC and WF-LSM, where there is only confocality in the *x* and *z* dimensions (see Fig. 7). However, in the case of WF-LSM and CL-LSM, the illumination NA is reduced, which allows for extended imaging along the z_i axis, at the cost of reduced image contrast compared to the corresponding DAC microscopy methods.

In terms of practical design considerations, it is apparent that there exist inherent tradeoffs between speed, contrast, and imaging depth for a potential DAC or LSM microscope. For example, due to point collection, PS-DAC offers the best contrast, but will have limited imaging speed due to the need to scan in 2D, whereas WF-LSM and CL-LSM offer the worst contrast, but enable fast imaging speeds and the ability to obtain 3D images with only 1D scanning. Therefore, the results in this study suggest that while the ultimate imaging depth may be reduced, volumetric superficial imaging in thick, highly scattering tissues is possible using either the WF-LSM or CL-LSM imaging geometry.

One limitation in the current study is the assumption of a homogenous scattering medium. Although this assumption is commonly made for optical Monte Carlo simulations in both the ballistic and diffuse regime, beam steering due to inhomogeneous scatterers (e.g. organelles, glands, and vascular structures) is a known phenomenon that is difficult to model in a traditional ray-tracing Monte Carlo simulation, but has been investigated using various alternative methods [27, 44–48]. In addition, note that our results assume that the imaging is limited by SBR (contrast) and not limited by SNR (a photon-limited situation). However, in certain cases, especially when imaging weak fluorescent structures, the imaging depth may be limited by insufficient signal (poor SNR), rather than too much background (poor SBR), and the optical throughput of the imaging system should therefore be considered. Finally, alternative illumination schemes other than the Gaussian beams modeled within this study have also been reported in the literature (structured illumination, Bessel and Airy beams, multi-photon, etc.) [49–52], which may be explored using similar methodologies in future studies.

Acknowledgments

The authors acknowledge funding support from the NIH/NIDCR R01 DE023497, and the NIH/NCI R01 CA175391.

#254248 Received 20 Nov 2015; revised 8 Jan 2016; accepted 9 Jan 2016; published 14 Jan 2016